Polycyclic Aromatic Hydrocarbons and Crystalline Silicates in the Bipolar Post-Asymptotic Giant Branch Star IRAS 16279-4757

Matsuura, M.; Zijlstra, A.A.; Molster, F.J.; Hony, S.; Waters, L.B.F.M.; Kemper, F.; Bowey, J.E.; Chihara, H.; Koike, C.; Keller, L.P.

DOI
10.1086/382064

Publication date
2004

Published in
Astrophysical Journal

The Astrophysical Journal, 604:791–799, 2004 April 1

POLYCYCLIC AROMATIC HYDROCARBONS AND CRYSTALLINE SILICATES IN THE BIPOLAR POST–ASYMPTOTIC GIANT BRANCH STAR IRAS 16279−4757[1,2]

M. Matsuura,[3] A. A. Zijlstra,[3] F. J. Molster,[4] S. Hony,[4] L. B. F. M. Waters,[5,6] F. Kemper,[7,8] J. E. Bowey,[9] H. Chihara,[10,11] C. Koike,[10] and L. P. Keller[12]

Received 2003 August 27; accepted 2003 December 16

ABSTRACT

IRAS 16279−4757 belongs to a group of post–asymptotic giant branch (post-AGB) stars showing both polycyclic aromatic hydrocarbon (PAH) bands and crystalline silicates. We present mid-infrared images that resolve the object for the first time. The morphology is similar to that of the "Red Rectangle" (HD 44179), the prototype object with PAHs and crystalline silicates. A two-component model and images suggest a dense oxygen-rich torus, an inner, low-density, carbon-rich region, and a carbon-rich bipolar outflow. The PAH bands are enhanced at the outflow, while the continuum emission is concentrated toward the center. Our findings support the suggestion that mixed chemistry and morphology are closely related. We discuss the *Infrared Space Observatory* Short-Wavelength Spectrometer (*ISO* SWS) spectra of IRAS 16279−4757. Several bands in the *ISO* SWS spectrum show a match with anorthite: this would be the first detection of this mineral outside the solar system. Compared to HD 44179, the shapes of PAH bands are closer to those of planetary nebulae, possibly related to a population of small PAHs present in HD 44179 but absent around IRAS 16279−4757. Detailed examination of the spectra shows the individual character of these two objects. The comparison suggests that the torus found in IRAS 16279−4757 may have formed more recently than that in HD 44179.

Subject headings: circumstellar matter — dust, extinction — infrared: stars — stars: AGB and post-AGB

1. INTRODUCTION

Some post–asymptotic giant branch (post-AGB) stars show both polycyclic aromatic hydrocarbon (PAH) and crystalline silicate bands in their infrared spectra. The formation history of this mixed chemistry (oxygen-rich silicates vs. carbon-rich PAHs) is not well understood. A possibility, although implausible, is that these stars all evolved from oxygen-rich to carbon-rich within the last few hundred years (Zijlstra et al. 1991). Waters et al. (1998) and Molster et al. (1999) proposed that the silicate dust is stored in a long-lived circumbinary disk. In this scenario, the PAHs form during a later mass-loss phase, after the star became carbon-rich, while the gas stored in the disk retains the chemistry of the earlier, oxygen-rich phase. Part of the amorphous silicate dust crystallizes in the disk. The scenario explains why there are relatively few post-AGB stars with this mixed chemistry and why the silicates have a lower temperature than the carbon-rich dust. It requires all such stars to be binaries, as is the case for the prototype of the class, the Red Rectangle (HD 44179; Waelkens et al. 1996).

IRAS 16279−4757 (hereafter IRAS 16279) is classified as a post-AGB star based on a double peak in its spectral energy distribution, which indicates a detached envelope (van der Veen, Habing, & Geballe 1989). Optical spectra suggest a spectral type of G5 (Hu et al. 1993). The *Infrared Space Observatory* Short-Wavelength Spectrometer (*ISO* SWS) spectra show crystalline silicates beyond 20 μm (Molster et al. 1999), and PAH bands are seen in the near-infrared (van der Veen et al. 1989) and *ISO* spectra. IRAS 16279 is therefore a member of the group of mixed-chemistry post-AGB stars.

We present TIMMI-2 mid-infrared imaging and spectroscopic data, resolving IRAS 16279 for the first time. In this paper we discuss the spatial distribution of the different dust components based on these images and compare these with predictions from the circumbinary disk scenario. We compare the spectra of this object with those of the prototype mixed-chemistry object, the Red Rectangle.

2. THE OBSERVATIONS

We obtained 10 and 18 μm images with TIMMI-2 (Käufl et al. 2000) at the ESO 3.6 m telescope on La Silla on 2003 May 27. The weather was clear with occasional cirrus clouds. We used six narrow *N*- and *Q*-band filters (Table 1). The diffraction limit is about 0.″7 (first null) in the *N* band and 1.″4 at the *Q* band. The optical seeing of 0.″8–1.″1 in FWHM allowed us to reach the diffraction limit in the images. The pixel scale is 0.″2. The background was subtracted with nodding and chopping with an offset of 15″. The pipeline-reduced data were used for imaging. The results from the aperture

[1] Based on observations with the European Southern Observatory 3.6 m telescope with TIMMI-2 at La Silla. The proposal number is 71.D-0049.

[2] Based on observations with *ISO*, an ESA project with instruments funded by ESA Member States (especially the PI countries: France, Germany, the Netherlands, and the United Kingdom) with the participation of the Institute of Space and Astronautical Science (ISAS, Japan) and NASA.

[3] Department of Physics, University of Manchester Institute of Science and Technology, P.O. Box 88, Manchester M60 1QD, UK.

[4] European Space Research and Technology Centre/European Space Agency (ESTEC/ESA), P.O. Box 299, 2200 AG Noordwijk, Netherlands.

[5] Astronomical Institute "Anton Pannekoek," University of Amsterdam, Kruislaan 403, 1098 SJ Amsterdam, Netherlands.

[6] Instituut voor Sterrenkunde, Katholieke Universiteit Leuven, Celestijnenlaan 200B, 3001 Heverlee, Belgium.

[7] Department of Physics and Astronomy, University of California, Los Angeles, CA 90095-1562.

[8] SIRTF Fellow.

[9] Department of Physics and Astronomy, University College London, Gower Street, London WC1E 6BT, UK.

[10] Kyoto Pharmaceutical University, Yamashina, Kyoto 607-8412, Japan.

[11] Department of Earth and Space Science, Osaka University, Toyonaka, Osaka 560-0043, Japan.

[12] NASA Johnson Space Center, Mail Code SR, Houston, TX 77058.

TABLE 1
FILTERS AND FLUX DENSITIES

Filter	$\lambda_{50\%\,\mathrm{cut}}$ (μm)	Flux (Jy)	Error (Jy)	Aperture (arcsec)
N7.9.....	7.42–8.11	23.4	4.8	4
N8.9.....	8.29–9.07	19.5	4.4	4
N9.8.....	9.10–10.02	20.0	4.5	4
N10.4.....	9.80–10.82	29.0	5.4	4
N11.9.....	10.99–12.19	59.8	7.7	6
Q.....	17.35–18.15	172	12	6

NOTE.—The last column lists the aperture used for photometry.

photometry are given in Table 1. The exposure time is about 16 minutes per image.

We also obtained 10 μm spectra with TIMMI-2, taken through a 1.2×50 arcsec^2 slit, oriented north-south. The slit was centered 0.″5 west from the brightest *N*-band position. The resolution is about 160 in $\lambda/\Delta\lambda$. The background was subtracted with 15″ chop-and-nod. We used Eclipse and IDL for the data reduction. The source extends approximately 6×8 arcsec^2, and the spectra are spatially resolved. The pixel scale of 0.″45 pixel^{-1} was binned to 0.″9 along the slit to increase the signal-to-noise ratio. The total exposure time is 58 minutes.

The flux calibration and the response/atmospheric transmission correction in the spectra were derived using HD 169916 (K1 III). The spectral template for HD 169916 is calculated by Cohen (1998).

We also use archival *ISO* SWS spectra, obtained on 1997 August 21 with a resolution of $\lambda/\Delta\lambda = 250-600$. The aperture is 14×27 arcsec^2 or larger, sufficient to cover the entire source. However, there are several flux discrepancies between the detector bands, probably due to a slight mispointing. We scaled the separate *ISO* SWS bands (12.45–27.29, 27.28–28.90, and 28.90–45.38 μm) so as to smoothly connect across the bands and to simultaneously agree with the *IRAS* broadband flux levels.

3. RESULTS

3.1. *Mid-Infrared Images*

The TIMMI-2 images of IRAS 16279 are shown in Figure 1. The object is clearly resolved in all images and more elongated within the PAH bands. This is clearly seen in Figure 2, in which we compare the intensity profiles of the various filters along the north-south axis with the profiles of a calibration star. To further quantify the spatial variations in the PAH and continuum emission, we show the PAH-to-continuum ratio (Figs. 3 and 4). The PAH emission is enhanced toward the southwest and northeast, giving the appearance of bipolarity. At the center, the PAH-to-continuum ratio is low. The elongated PAH emission distribution and the low PAH/continuum ratio at the center are similar to what is found in the Red Rectangle (Waters et al. 1996).

To confirm that the PAH images are more elongated than the continuum images, we fitted the images with two two-dimensional Gaussian functions. The first Gaussian component represents the bright core, and the second Gaussian measures the intensity and elongation direction of the faint extended emission. The peak positions of the two Gaussian profiles are fixed at the same place. The best-fit parameters are summarized in Table 2. The PAH bands (N7.9, N8.9, and N11.9) show a relatively stronger second component (larger a_2/a_1 ratio), confirming the extended appearance in these bands.

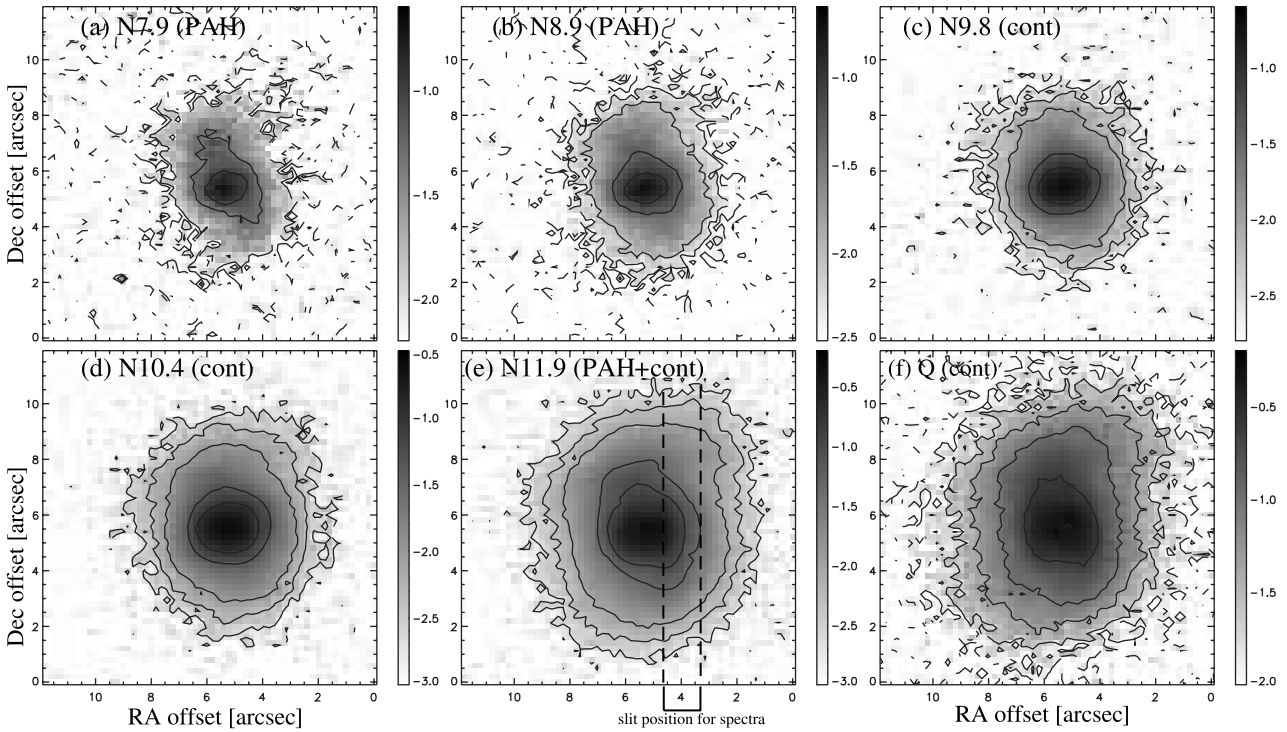

FIG. 1.—Images of IRAS 16279−4757 in units of $\log F_\nu$ in Jy pixel^{-1}. The object is elongated, especially in the PAH bands. Contour lines show 0.0025, 0.005, 0.01, 0.05, and 0.1 Jy pixel^{-1} for the *N* band, and 0.01, 0.025, 0.05, 0.1, 0.25, and 0.5 Jy pixel^{-1} for the *Q* band. The dashed lines in (*e*) show the approximate slit position for the spectra.

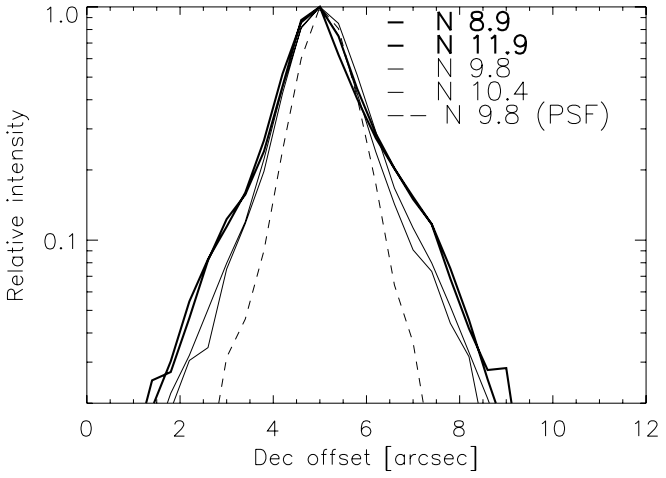

FIG. 2.—Intensity profiles in declination, across the source center (corresponding to R.A. offset = 5″.6 in Fig. 1). The peak intensity is normalized to unity. The profiles of the N8.9 and N11.9 bands, which cover PAH features, are shown in bold: they have longer tails than the continuum bands (N9.8 and N10.4; *thin lines*). The profile of the calibration star (HD 169916) at the N9.8 band is shown as the dashed line.

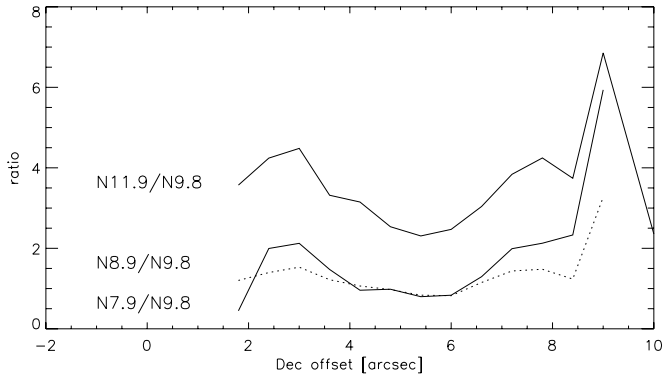

FIG. 4.—Intensity ratio of the PAH bands with respect to N9.8 (pseudo-continuum) along declination through the source center (R.A. offset = 5″.6). The data are smoothed to a 0″.4 grid. The approximate error levels are about 0.8–1.0.

The *Q*-band and N11.9 images (Fig. 1) show a more rectangular shape, slightly elongated both along the southwest-northeast direction (as found in PAH images) and the southeast-northwest direction. The rotation angles change from 160° in the 10 μm bands, to 75° at 11.9 μm, to 10° at 18 μm. The *Q*-band filter contains mainly dust continuum (§ 3.3). Although the N11.9 band contains a PAH feature, this contributes only about 1/2–1/3 of the intensity, and the rest is continuum. This rectangular shape might also be present in other continuum images; however, the emission is fainter in the shorter wavelength continuum bands.

3.2. *TIMMI-2 Spectra*

The *N*-band spectra (Fig. 5) show PAH bands at 7.7, 8.6, and 11.2 μm. The weaker 12.7 μm PAH band (e.g., Cohen, Tielens, & Allamandola 1985; Hony et al. 2001) is also detected in IRAS 16279. The spatially resolved *N*-band spectra show that the central spectrum (actually 0″.5 west of the brightest position) has the strongest continuum, while the strongest 11.2 μm PAH band is found 0″.9 south (see also Fig. 6). The spectrum 0″.9 north shows only a weak PAH feature. The line-to-continuum ratio is lower at the center than at 0″.9 south, in agreement with the ratio images displayed in Figure 3.

The lower PAH-to-continuum ratio at the center (Figs. 3 and 4) is due to the fact that the continuum intensity declines sharper than the PAH intensity along the southwest-northeast direction (Fig. 6). The PAH intensity itself is still reasonably high near the center, as seen in spectra.

3.3. *Modeling the ISO SWS Spectra*

In order to obtain a globally consistent physical picture of the source, we model the *ISO* SWS spectrum. We show the full 2.3–45 μm spectrum in Figure 7. Most of the detected energy falls in the infrared range and thus originates from the circumstellar dust. The peak wavelength of the energy distribution (∼30 μm) implies a typical dust temperature of about 100 K. Below 15 μm the spectrum is dominated by C-rich material, while beyond 20 μm the solid-state features can be attributed to crystalline silicates.

We use a spherically symmetric model consisting of two distinct $n \propto r^{-2}$ regions, one containing carbon dust and PAHs, and the other containing silicate dust. The model is described in Siebenmorgen & Krügel (1992) and Siebenmorgen, Zijlstra, & Krügel (1994): it is a one-dimensional model that includes scattering and transient heating. The radiative transfer is solved independently for the carbon-rich and the oxygen-rich regions. We do not include the possible effect of the fairly

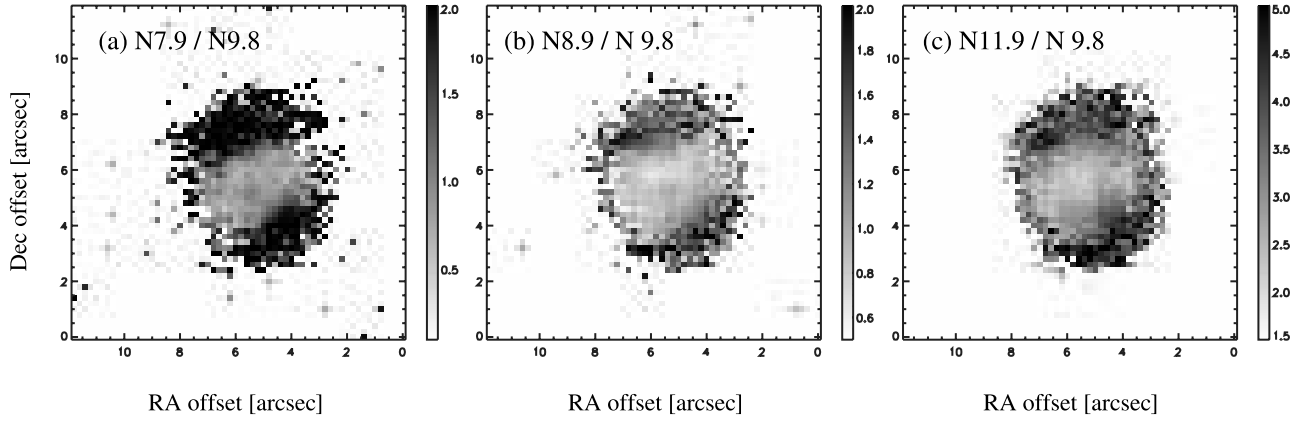

FIG. 3.—Intensity ratios of the PAH bands with respect to the continuum (N9.8). The PAH is enhanced in the outflows.

TABLE 2
FITTED RESULTS OF THE IMAGES WITH TWO TWO-DIMENSIONAL GAUSSIAN PROFILES

Filter	$\sigma_{1\,\mathrm{maj}}$ (arsec)	$\sigma_{1\,\mathrm{min}}$ (arsec)	a_1 (Jy pixel^{-1})	θ_1 (deg)	$\sigma_{2\,\mathrm{maj}}$ (arsec)	$\sigma_{2\,\mathrm{min}}$ (arsec)	a_2 (Jy pixel^{-1})	θ_2 (deg)	a_2/a_1
N7.9.....	1.28	0.84	0.122	152.7	1.79	0.84	0.034	136.9	0.279
N8.9.....	0.66	0.40	0.117	79.5	1.64	1.06	0.056	158.0	0.479
N9.8.....	0.73	0.57	0.163	82.0	1.84	1.35	0.025	166.5	0.153
N10.4.....	0.74	0.58	0.198	81.9	1.67	1.29	0.048	167.3	0.242
N11.9.....	0.69	0.52	0.322	86.0	1.64	1.17	0.135	74.5	0.419
Q.....	1.10	0.79	0.266	146.1	2.39	1.73	0.213	8.4	0.801

NOTES.—The value a is the peak intensity. The values σ_{maj} and σ_{min} are along the major and minor axes, respectively. The value θ is the rotation angle of the major axis with respect to north (clockwise). The subscripts 1 and 2 show each Gaussian component ($a_1 > a_2$). The first component measures the bright core region, and the second component shows the more extended emission. The first component in N7.9 is strongly affected by the extended component, and θ_1 is totally different from those in other bands.

low extinction within the carbon-rich region on the heating of the (outer) oxygen-rich region.

The distance and extinction are derived assuming a luminosity of $1 \times 10^4\ L_\odot$. The integrated flux (optical-to-infrared photometry from Hu et al. 1993, Van de Steene, van Hoof, & Wood 2000, *IRAS*, and *ISO*) gives a distance estimate of 2.0 kpc. IRAS 16279 is in the Galactic plane ($b = +0\overset{\circ}{.}09$) and will suffer interstellar extinction. The optical photometry is reported as $R = 18.42$ and $I = 14.57$ mag (Hu et al. 1993). For a spectral type of G5 (Hu et al. 1993), we derive $A_V = 14.8$ mag. Six field stars within $30'$ show an interstellar extinction of 1.0 mag kpc^{-1} out to 1.3 kpc. This suggests an interstellar extinction of $A_V \sim 2.0$ mag. Most of the large extinction of IRAS 16279 is likely of circumstellar origin. Therefore, we ignore the interstellar extinction in the model fit.

Figure 7 shows the fitted result. Up to 10 μm, the emission from carbon material is the dominant source of continuum emission. The oxygen shell begins to contribute at 11 μm and is dominant beyond 15 μm. The derived parameters (Table 3) show that most of the dust is actually cold oxygen-rich dust: the carbon region is much less dense and contributes little to the mass.

Table 3 shows that the carbon-rich gas is mostly located inside the oxygen-rich region. Both regions have a covering factor (sky coverage as seen from the central star) of about 30%–35%. The precise value depends on the choice of parameters, but all fits we obtained required that the output infrared flux be scaled down by at least half. The derived covering factors and the bipolar morphology in the images suggest that the different dust components may be located in different directions from the star. The model is consistent with an oxygen-rich torus, where we assume that the radial density distribution is the same everywhere within the torus.

The major PAH bands can be reasonably fitted with the model, except for the one at 8.6 μm (this problem is also found by Siebenmorgen et al. 1994). The oxygen shell gives less than half the observed A_V and makes a weaker silicate absorption feature than the observed one (seen against the carbon continuum): the remainder may be due to interstellar absorption or to geometrical effects. The 10 μm absorption is seen mainly against the inner arcsecond carbon-rich dust. For a r^{-2} shell, the

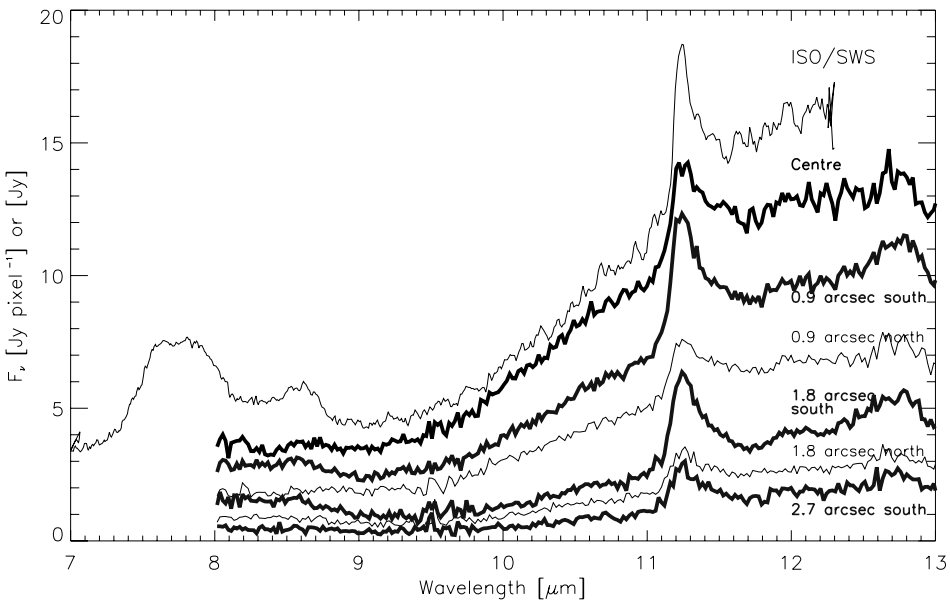

FIG. 5.—*N*-band spectra with TIMMI-2, compared to *ISO* SWS spectra. The slit position of TIMMI-2 is R.A. offset $\sim 4\overset{''}{.}0$, which crosses the southwest PAH-enhanced region. Flux units of the TIMMI-2 spectra are in Jy pixel^{-1}. The *ISO* SWS spectra are in Jy but are scaled by 1/3. The 11.2 μm PAH feature is strong in the spectra located $0\overset{''}{.}9$ south and changes its shape from north to south.

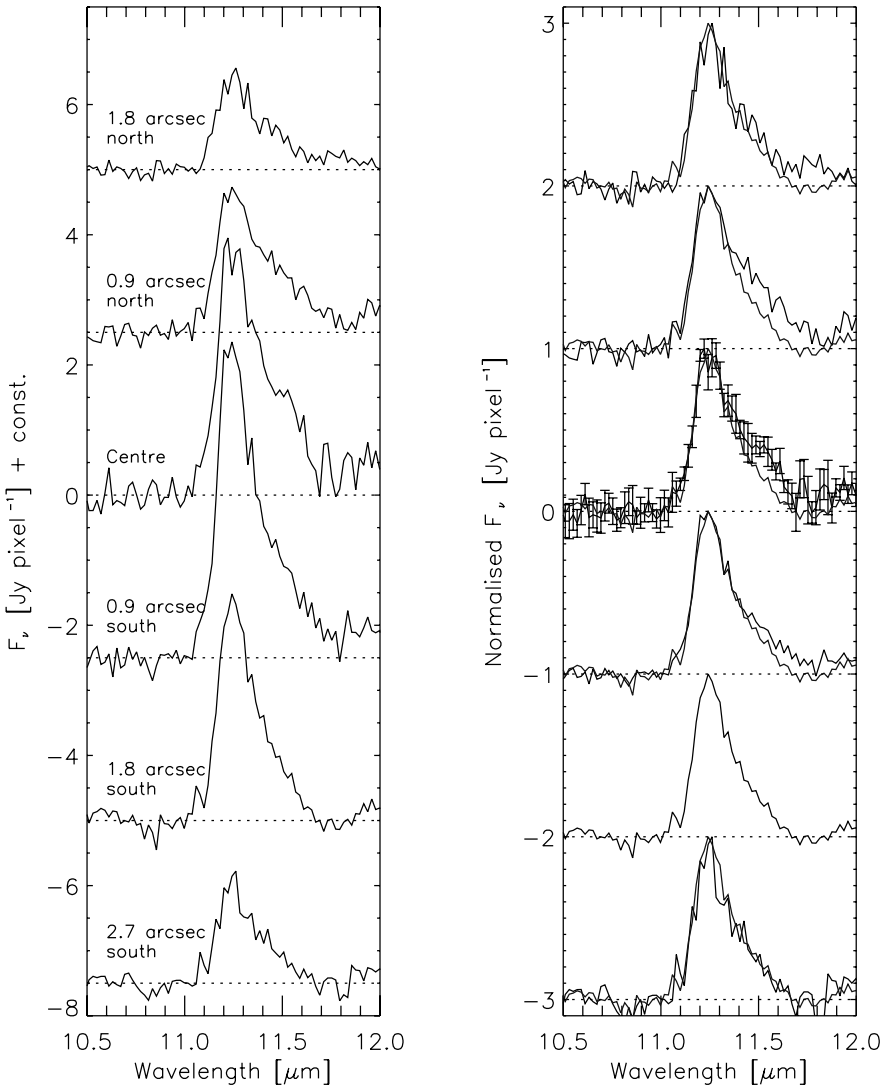

FIG. 6.—*Left*: 11.2 μm PAH feature after subtraction of the continuum. The continuum is estimated using a linear fit between 10.5–11.0 and 11.9–12.4 μm. The PAH feature is strongest at the southwest outflow (0.″9 south). *Right*: To examine the variation in the shape, the individual spectra are normalized to the peak intensity. We plot the spectra at 1.″8 south in gray lines as references. Near the center, the feature is broader at the red wing of the 11.2 μm feature. The error at certain wavelengths is estimated from the standard deviation of the nearby 5 pixels with the same wavelength in target and calibration data.

tangential line of sight can have a much higher extinction, and depending on the viewing angle, this can affect the carbon-rich region. The one-dimensional nature of the model means that self-absorption within the dust regions is not well described. The line of sight to the star also shows higher extinction, but it is clear that a global one-dimensional model may well underestimate the column density in individual lines of sight.

The carbon-rich shell has an outer radius of 5×10^{16} cm (1.″8) in the model, which is close to the $\sigma_{2\mathrm{maj}}$ measured in the PAH bands. The inner radius of the carbon-rich shell is 1×10^{16} cm (0.″3). The inner radius is not clearly seen in the image because the spatial resolution is not high enough and because the point-spread functions of the central star and the shell are merged.

The model fitting yields several constraints:

1. To excite the PAH, the model requires a stellar temperature of 6000 K or more; otherwise, the bands disappear because of the lack of exiting photons. This includes absorption by neutral PAHs. The PAH emission features are thought to arise from the mixture of neutral and charged PAHs. PAH ions can absorb in the optical (cf. Li & Draine 2002), and this would allow a lower stellar temperature. Li & Draine (2002) show that weak PAH bands can be seen for stellar temperatures as low as 3000 K but reach full strength only above 6000 K. In addition, the presence of the 11.2 μm feature, which attributes to neutral PAHs (Hony et al. 2001), suggests that UV radiation is necessary and that extremely low temperature is not possible. The observed PAH bands are compatible with a G-type central star.

2. The PAH bands are only seen in relatively unshielded (low-extinction) gas. Within the model, only a low-density shell contributes to the PAH bands. Higher density carbon regions, if present, would not contribute to the observed PAH bands: the excitation of the PAHs would be suppressed by internal extinction. We therefore have few constraints on higher density carbon-rich gas.

3. The oxygen-rich gas is located relatively far out (inner radius of 1″) and has much higher mass than the carbon-rich

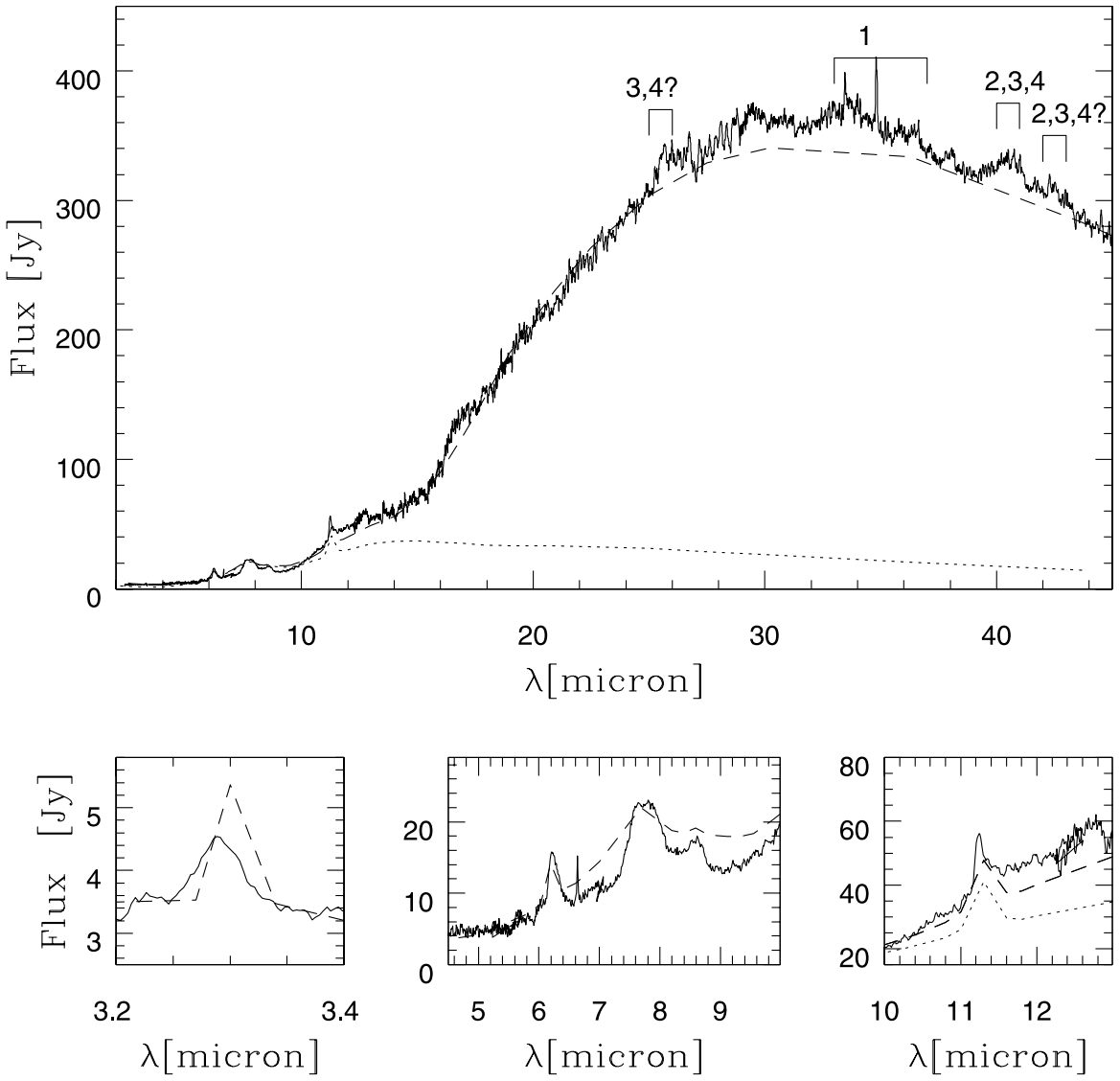

FIG. 7.—*ISO* SWS spectra. The numbers show the identifications of crystalline silicate bands: 1 = forsterite + plateau, 2 = enstatite, 3 = diopside, and 4 = anorthite. Emission lines at 6.63 and 34.8 μm could be due to C I. The dashed line is the two-component model described in the text. The dotted line represents the continuum component of the model spectra due to the carbon grains only. The spectra of PAH features are enlarged in the bottom.

gas. The low temperatures of this gas are consistent with the observed crystalline silicate bands (70–110 K; see § 4.2).

4. DUST FEATURES

The *N*-band images clearly show that the PAH emission originates from a bipolar geometry. This further strengthens the link between this source and HD 44179 and the link between the mixed-chemistry nature and a bipolar (+ disk) geometry. It is interesting to further explore the comparison between IRAS 16279 and the Red Rectangle as the prototype of the dual chemistry sources. In the following we compare the PAH emission features between the two sources and present a detailed comparison of the crystalline silicate bands.

TABLE 3
MODEL PARAMETERS OF THE TWO-SHELL MODEL

Parameter	C Shell	O Shell
r_{in} (cm)	1×10^{16}	4×10^{16}
r_{out} (cm)	5×10^{16}	8×10^{16}
M_{shell} ($M_\odot$)	3×10^{-3}	2.1
A_V (mag)	0.6	6.4
T_d (K)	330–140	125–57
Coverage (%)	30	35

4.1. *PAH Bands*

4.1.1. *Integrated Spectrum*

In Figure 8 we show the *ISO* PAH spectra of IRAS 16279, HD 44179, as the prototype of the mixed-chemistry post-AGB stars and CD $-42^\circ 11721$ as a prototypical interstellar medium (ISM) star-forming region PAH spectrum. The profile features are very similar in the 3 μm and the 10–13 μm regions (C-H modes), while large differences are found in the PAH spectrum from 6 to 9 μm (C-C modes). This strong variation in the 6–9 μm PAH bands, when compared to the other PAH bands, is a common feature of the interstellar PAH spectra (B. van Diedenhoven et al. 2004, in preparation). The profiles of the

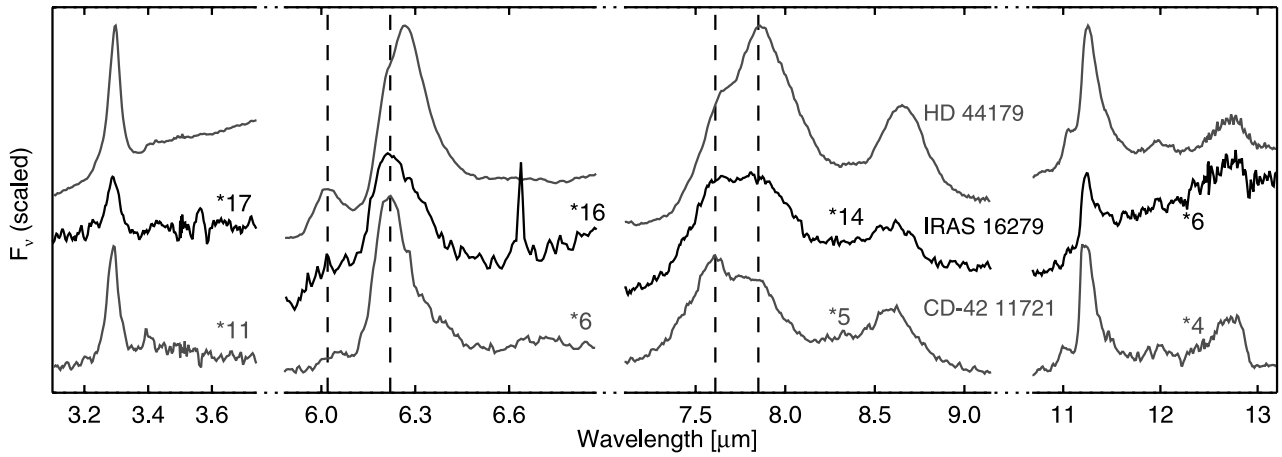

FIG. 8.—Comparison between the PAH bands in the *ISO* SWS spectra of HD 44179, IRAS 16279, and the reflection nebulosity near CD −42°11721 (*top to bottom*). The dashed lines indicate where the IRAS 16279 spectrum differs most from the ISM PAH spectrum (as represented by CD −42°11721) and HD 44179. The spectra are binned to a resolution of $\lambda/\Delta\lambda = 200$.

6–9 μm PAH bands of IRAS 16279 are intermediate between HD 44179 and CD −42°11721 (Peeters et al. 2002). The 6.2 μm feature of IRAS 16279 is broader than that in CD −42°11721. This broadening is due to an extra contribution near 6.05 μm, which is also present in HD 44179, and a weak emission band, which peaks near 6.28 μm. The latter band is dominant in the spectrum of HD 44179 yet only marginally detected in IRAS 16729, where the usual 6.22 μm band is the strongest.

The PAH bands from 7 to 9 μm (regularly dubbed the "7.7 complex") also attest to the intermediate nature of IRAS 16279 PAH emitters. In the ISM and in star-forming regions, the 7.6 μm band is usually dominant, while in planetary nebulae and post-AGB stars, the 7.8 μm band is strongest (Bregman 1989; Cohen et al. 1989; Peeters et al. 2002). In IRAS 16279 both bands are roughly equally strong.

Hony et al. (2001) found that the band strength ratio of the 11.2–12.7 μm bands ($I_{11.2}/I_{12.7}$, where $I_{11.2}$ and $I_{12.7}$ represent the integrated flux of each band) correlates with the source type. In the planetary nebulae this ratio is very high, as is the case for HD 44179 ($I_{11.2}/I_{12.7} = 5.0$). The band strength ratio found in IRAS 16279 ($I_{11.2}/I_{12.7} = 2.0$) is not typical for evolved stars.

When comparing the band strength of the 3.3 μm band with the longer wavelength PAH bands, we find that the 3.3 μm of IRAS 16279 is much weaker than in HD 44179. The ratios of the integrated band strengths, $I_{11.2}/I_{3.3}$, are 1.9, 5.2, and 3.9 in HD 44179, IRAS 16279, and CD −42°11721, respectively. The ratios of IRAS 16279 are closer to CD −42°11721. This may point to a population of smaller PAHs around HD 44179, which does not exist around the other two sources. Such small PAHs might be easily destroyed when exposed to the hard UV radiation present in the ISM and planetary nebulae.

4.1.2. *Spatially Resolved Spectroscopy*

In Figure 6 we show the profile of the 11.2 μm band as extracted from the *N*-band spectra for different positions. On the right we compare the normalized profiles. The profile varies with the position along the slit, being broader at the central position and 0.″9 north. A longer tail at 11.5 μm is usually interpreted as being due to hotter PAHs (Tielens et al. 1999; Pech, Joblin, & Boissel 2002). Alternatively, a different profile might arise from a variation of the PAH population as a function of distance to the source. For example, PAHs with two neighboring C-H bonds may give rise to emission in the red wing of the 11.2 μm solo C-H mode (Hony et al. 2001). We prefer the hot PAH interpretation because the sharp blue-side rise stays the same in the all spectra, which is difficult to envisage in the scenario of a strongly varying PAH population. Furthermore, the most pronounced tail is found closest to the central star, where multiple photon heating may play a role and therefore hotter PAHs might be expected.

Miyata et al. (2001) show spatially resolved *N*-band spectra of HD 44179, in which they also find variations of the emission features as a function of distance to the star. As in IRAS 16279, the 11.2 μm band diminishes close to the central star. However, unlike in IRAS 16279, the HD 44179 spectrum near the central star is dominated by bands at ∼11.0 and ∼11.9 μm. These bands could be related to the crystalline enstatite that is present in the disk. Because of this possible confusion between the different contributors to the emission in HD 44179, it is not feasible to determine the band profile of the 11.2 μm nearest the central star.

In conclusion, we can state that there are significant differences in the PAH spectrum of HD 44179 and IRAS 16279, both in band strength ratios and profile features, where the latter source exhibits an PAH spectrum intermediate between HD 44179 and the prototypical ISM PAH spectrum. In this sense the PAH spectrum of IRAS 16279 compares better, in band strengths and feature profiles, with the young C-rich planetary nebulae IRAS 21282+5050 (Hony et al. 2001; Peeters et al. 2002).

4.2. *Crystalline Silicate Bands*

The *ISO* SWS spectra beyond 20 μm show the solid-state features that are attributed to crystalline silicates (Fig. 7). Continuum-subtracted spectra are shown in Figure 9. The continuum is obtained with a quadratic fit (polynomial fit to the three neighboring points) to the smoothed spectra.

The feature at 33.7 μm has been identified with crystalline olivine ($Mg_{2x}Fe_{2-2x}SiO_4$, with x between 0 and 1). Its position fits best with that of the pure Mg-olivine, i.e., forsterite (Mg_2SiO_4: Waters et al. 1996; Molster, Waters, & Tielens

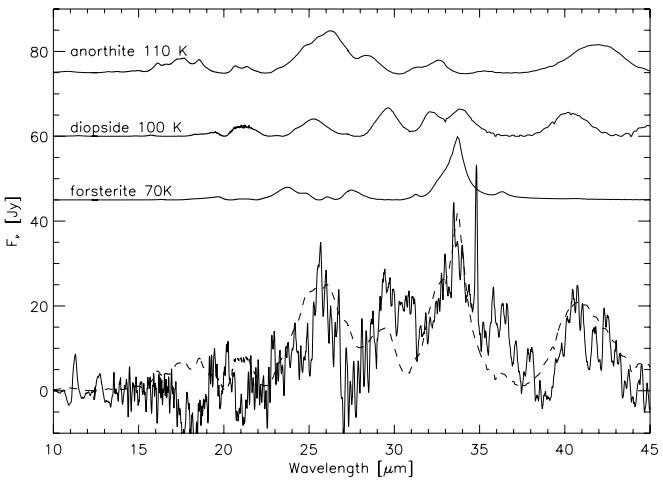

FIG. 9.—Continuum-subtracted ISO SWS spectra (*solid line*). The dashed line shows the fitting of the crystalline bands (Molster et al. 2002b). The dust properties are measured by Koike et al. (1999, 2000) and H. Chihara et al. (2004, in preparation).

2002a). The band ratio depends on the temperature (Molster 2000, p. 14). The absence of a feature around 23.7 μm shows that forsterite is below 100 K. The plateau up to 37 μm, which has no clear mineralogical identification, is prominent in this star.

The feature at 40.5 μm is normally attributed to pyroxene-like silicates ($MSiO_3$, where M stands for metal). The presence of features also around 43 μm is normally an indication for the presence of enstatite ($MgSiO_3$). However, the lack of enstatite features below 30 μm makes this identification questionable. The *ISO* SWS band 3E (27.5–29 μm) is known for its mediocre performance. This could explain the lack of enstatite features around 28 μm. Alternatively, enstatite could also simply be very cold, like the forsterite. Whatever the reason, it should be noted that the 40.5 μm feature is rather strong with respect to the 43 μm feature if it is purely due to enstatite. This implies that more materials might be present.

There are some other features present around 26, 29, and 32 μm. These three positions, together with the 40.5 μm feature, could fit with the features of diopside ($CaMgSi_2O_6$) measured in the laboratory (Koike et al. 2000). The slight wavelength shift around 26 and 40.5 μm with respect to the laboratory and, in addition, the lack of a clear feature around 21 μm, make the identification less conclusive. But these differences might be explained by temperature and grain size and shape effects, as is also observed for other silicates, such as forsterite (Bowey et al. 2002; Molster et al. 2002a, 2002b).

Another mineral that might explain some of the features is anorthite. Properties of anorthite have been measured in the laboratory (H. Chihara, C. Koike, & A. Tsuchiyama 2004, in preparation; L. Keller et al. 2004, in preparation). The profile presented in Figure 9 is for a sample of An_{96} in H. Chihara et al. (2004, in preparation). It matches with the feature at 26 μm, the long-wavelength side of the 40 μm complex, and the extra feature just before the 33.7 μm forsterite feature. This would be the first identification of anorthite outside the solar system. The lack of anorthite features in the *ISO* spectrum around 18 μm might be explained by low temperature or interstellar absorption.

We would require future spectra beyond 45 μm to confirm the presence of anorthite and diopside, which have stronger bands in these wavelengths. We should also stress here that we are dealing with an artificial continuum, and this can have some influence on the strength of the features.

5. DISCUSSION

The mid-infrared images of IRAS 16279 show an elongation in the PAH band and a rectangular shape in the N11.9 and *Q*-band images. At the center, the PAH-to-continuum ratio decreases. There is some resemblance to the Red Rectangle (HD 44179; Waters et al. 1998). In the Red Rectangle, the silicates are thought to be located in a disk and the PAHs are in the perpendicular polar flows. The images of IRAS 16279 strengthen this link between morphology and mixed chemistry, as proposed by Waters et al. (1996) and Molster et al. (1999).

The temperature of the crystalline silicate bands in HD 44179 is about 135 K (enstatite; Molster et al. 2002b), while it is below 110 K in IRAS 16279. Nevertheless, both objects show a lower temperature in the silicates than in the PAH region. In fact, all crystalline silicates in post-AGB stars tend to show low temperatures (100–250 K; Molster et al. 2002b).

In the case of IRAS 16279, the model suggests that the PAH emission in the southwest and northeast regions (Fig. 1) cannot be shielded by the dusty oxygen-rich regions. The oxygen-rich material should be configured as a torus rather than a shell, which allows radiation to leak toward the southwest and northeast directions. The model explains the PAH excess at 2″: the decreasing temperature suppresses the continuum but not the PAH bands.

This structure, with a low-density carbon-rich region and an obscured, dense, oxygen-rich torus, agrees with the (Red Rectangle) oxygen-rich disk scenario of Waters et al. (1996) and Molster et al. (1999). But the oxygen-rich region in IRAS 16279 is several times larger than that seen in the Red Rectangle. A circumbinary disk is expected to be compact in order to store the oxygen-rich gas over a long period. It is not clear whether this has happened in IRAS 16279. The extended torus should disrupt faster than the disk of the Red Rectangle. Its formation may have happened relatively recently.

The crystallization of amorphous silicates occurs via the heating and subsequent cooling of the grain. This may occur slowly at low temperature in a long-term stable disk, under the influence of UV radiation (as in the Red Rectangle), or quickly in the AGB wind at very high mass-loss rates, through high-temperature annealing (Waters et al. 1996; Sylvester et al. 1999). Assuming an expansion velocity of 20 km s^{-1}, the mass-loss rate of IRAS 16279 was of order $5\times 10^{-4}\ M_\odot\ yr^{-1}$, sufficient for high-temperature annealing in the outflow to occur. Therefore, crystallization itself may have occurred already in the AGB outflow. Part of the crystallized silicate is stored in the disk later, and part of it may remain in the outflow.

It is not clear that the torus is stable long enough for long-term crystallization. This may be solved by shocks addressed by Harker & Desch (2002), who found that a 5 km s^{-1} shock is sufficient for annealing in the comets. This velocity range might be possible in AGB or post-AGB wind interaction with the torus. In this case, the higher density of the torus is more likely to obtain a higher rate of crystallization, and this may compensate for the short lifetime of the torus compared to the disk.

The crystalline silicate bands in IRAS 16279 are significantly weaker than in HD 44179 (Waters et al. 1998).

The weakness of the features indicate that either they are less abundant than in HD 44179, or the temperature difference with the hotter amorphous silicates (responsible for the continuum) is larger in IRAS 16279. Although a difference in abundance clearly cannot be excluded, the low temperature of the crystalline silicates seems to be supported by the absence of detectable features below 30 μm.

We are grateful for the support from ESO staff members during the TIMMI-2 observations, especially V. Doublier and F. Comeron. We acknowledge G. C. Van de Steene and H. van Winckel for the discussion of Brγ in this object. We thank ESA for maintaining the *ISO* data archives and *ISO* SWS data. M. M. and J. E. B. are financially supported by PPARC, and F. K. is supported by NASA through the SIRTF Fellowship Program, under award 011 808-001.

REFERENCES

Bowey, J. E., et al. 2002, MNRAS, 331, L1
Bregman, J. 1989, in IAU Symp. 135, Interstellar Dust, ed. L. J. Allamandola & A. G. G. M. Tielens (Dordrecht: Kluwer), 109
Cohen, M. 1998, AJ, 115, 2092
Cohen, M., Tielens, A. G. G. M., & Allamandola, L. J. 1985, ApJ, 299, L93
Cohen, M., et al. 1989, ApJ, 341, 246
Harker, D. E., & Desch, S. J. 2002, ApJ, 565, L109
Hony, S., Van Kerckhoven, C., Peeters, E., Tielens, A. G. G. M., Hudgins, D. M., & Allamandola, L. J. 2001, A&A, 370, 1030
Hu, J. Y., Slijkhuis, S., de Jong, T., & Jiang, B. W. 1993, A&AS, 100, 413
Käufl, H. U., et al. 2000, Messenger, 102, 4
Koike, C., et al. 1999, in Proc. 32nd ISAS Lunar and Planetary Symp., ed. H. Mitzutani & M. Kato, 175
———. 2000, A&A, 363, 1115
Li, A., & Draine, B. T. 2002, ApJ, 572, 232
Miyata, T., et al. 2001, in Post-AGB Objects as a Phase of Stellar Evolution, ed. R. Szczerba & S. K. Górny (Dordrecht: Kluwer), 351
Molster, F. J. 2000, Ph.D. thesis, Univ. Amsterdam
Molster, F. J., Waters, L. B. F. M., & Tielens, A. G. G. M. 2002a, A&A, 382, 222
Molster, F. J., Waters, L. B. F. M., Tielens, A. G. G. M., Koike, C., & Chihara, H. 2002b, A&A, 382, 241
Molster, F. J., et al. 1999, Nature, 401, 563
Pech, C., Joblin, C., & Boissel, P. 2002, A&A, 388, 639
Peeters, E., Hony, S., Van Kerckhoven, C., Tielens, A. G. G. M., Allamandola, L. J., Hudgins, D. M., & Bauschlicher, C. W. 2002, A&A, 390, 1089
Siebenmorgen, R., & Krügel, E. 1992, A&A, 259, 614
Siebenmorgen, R., Zijlstra, A. A., & Krügel, E. 1994, MNRAS, 271, 449
Sylvester, R. J., Kemper, F., Barlow, M. J., de Jong, T., Waters, L. B. F. M., Tielens, A. G. G. M., & Omont, A. 1999, A&A, 352, 587
Tielens, A. G. G. M., Hony, S., van Kerckhoven, C., & Peeters, E. 1999, The Universe as Seen by *ISO*, ed. P. Cox & M. F. Kessler (ESA-SP 427; Noordwijk: ESA), 579
Van de Steene, G. C., van Hoof, P. A. M., & Wood, P. R. 2000, A&A, 362, 984
van der Veen, W. E. C. J., Habing, H. J., & Geballe, T. R. 1989, A&A, 226, 108
Waelkens, C., Van Winckel, H., Waters, L. B. F. M., & Bakker, E. J. 1996, A&A, 314, L17
Waters, L. B. F. M., et al. 1996, A&A, 315, L361
———. 1998, Nature, 391, 868
Zijlstra, A. A., Gaylard, M. J., te Lintel Hekkert, P., Menzies, J. W., Nyman, L.-A., & Schwarz, H. E. 1991, A&A, 243, L9